Solar RRL
www.solar-rrl.com

Optimizing Aesthetic Appearance of Perovskite Solar Cells Using Color Filters

Jonas Schaible, Hanifah Winarto, Viktor Škorjanc, Danbi Yoo, Lea Zimmermann, Klaus Jäger, Ivan Sekulic, Philipp-Immanuel Schneider, Sven Burger, Andreas Wessels, Benedikt Bläsi, and Christiane Becker**

The significance of color aesthetics in photovoltaic (PV) modules gains importance, especially in design-centric applications like building-integrated PVs. Color filters based on distributed Bragg reflectors, consisting of alternating thin-film layers of different refractive indices, can modify the appearance of standard silicon modules. This approach is also extended to optimize the color appearance of emerging PV technologies such as perovskite solar cells, which typically exhibit a less appealing gray–brownish appearance. In this contribution, perovskite solar-cell stacks combined with MorphoColor color filters are presented. Angular-resolved reflectance simulations based on wave optics and ray tracing with experimental data are validated, and the color appearance from various viewing angles is evaluated. Additionally, the impact of individual layers on color appearance and the maximum achievable short-circuit current density in the perovskite solar cell is investigated. By applying Bayesian optimization, the color distance is minimized to the targeted appearance. Tailoring the bridging layers between the color filter and the perovskite solar cell is found to strongly influence the color impression due to the coherently combined color filter and perovskite solar cell. The presented color optimization concept allows to customize the aesthetics of emerging PV thin-film technologies such as perovskite solar cells.

1. Introduction

Aesthetic aspects are playing an increasingly important role in photovoltaics (PVs) due to the accelerated expansion of solar power in urban and rural environments. The combination of the large construction and PV markets offers great potential for building-integrated PVs (BIPV).[1] Although various BIPV products are available on the EU market (>200), their adoption rate remains at 1%–3% of all PV installations. The vast majority of BIPV projects (90%) use solutions which replace a single component, e.g., the cladding of a building, in a manner compatible with traditional material solutions. The same is true for the building design, which follows mainly traditional architecture.[2] Camouflaged BIPV solutions can help increase the adoption rate of PV in urban environments. Since aesthetics play a crucial role in the adoption and acceptance, their optimization is of importance.

In recent years, there have been strong efforts to improve the color appearance of PV modules. Comparisons of approaches can be found in refs. [3,4]. According to these references, the approximate ranges of relative losses for the most relevant technologies are 8%–30% for printed glass, 6%–20% for colored encapsulants, and 4%–10% for interference coatings, including MorphoColor.[5] For optical interference filters that are directly implemented into the cover glass, the influence of filter design factors, such as material composition, refractive index, and geometry, on efficiency and color appearance parameters—including achievable Lightness, Chroma, Hues, and angular color dependence—has been studied in detail.[5–10] Further, simulation studies on theoretically achievable efficiency limits and color appearance for single- and multi-junction PVs have been made.[11,12] These color filters are very promising as they allow for a saturated color appearance, a high tolerance with respect to the viewing angle, low

J. Schaible, H. Winarto, V. Škorjanc, D. Yoo, L. Zimmermann, K. Jäger, C. Becker
Division Solar Energy
Helmholtz-Zentrum Berlin für Materialien und Energie GmbH
12489 Berlin, Germany
E-mail: jonas.schaible@helmholtz-berlin.de;
christiane.becker@helmholtz-berlin.de

J. Schaible, K. Jäger, I. Sekulic, P.-I. Schneider, S. Burger
Zuse Institute Berlin
Takustraße 7, 14195 Berlin, Germany

The ORCID identification number(s) for the author(s) of this article can be found under https://doi.org/10.1002/solr.202400627.

DOI: 10.1002/solr.202400627

I. Sekulic, P.-I. Schneider, S. Burger
JCMwave GmbH
Bolivarallee 22, 14050 Berlin, Germany

A. Wessels, B. Bläsi
Fraunhofer-Institut für Solare Energiesysteme ISE
79110 Freiburg, Germany

C. Becker
Faculty 1: School of Engineering – Energy and Information
Hochschule für Technik und Wirtschaft Berlin
10313 Berlin, Germany

power conversion efficiency (PCE) losses, and fabrication on a square-meter basis by sputtering[8,9] and recently also inkjet printing.[13] In the field of emerging PV technologies, such as perovskite solar cells, research on aesthetic appearance has only recently started. The less appealing appearance of perovskite devices, which often exhibit a gray–purple–brownish color, requires control of the aesthetics, especially for BIPV solutions.

Lately, various ways of coloring perovskite solar cells were studied that can be classified in opaque and transparent appearances, e.g., for colored windows. Heo et al. studied bifacial colored perovskite solar cells using tunable transparent electrodes.[14] Despite achieving reflectance fractions below 20% and observing relative PCE losses ranging from 5% to 16%, the resulting color exhibits low saturation, resulting in muted Hues. Bae et al. studied colored opaque perovskite solar cells using cholesteric helicoidal superstructures.[15] They report on high PCEs and simple design and fabrication processes due to the use of organic components and wet chemical processes. However, its iridescent reflection results in limited color stability. Angle-invariant color perception and precise control of color appearance are achieved through inkjet-printed colorization of perovskite solar cells, as shown by Eggers et al.[16] They report not only bright colors but also 30% PCE loss compared to reference devices. Yoo et al.[17] followed an approach using nonperiodic SiO_2/TiO_2 multi-nanolayer filters on solar glass. Only 6%–10% reduction of PCE compared to the noncolored reference and an increased photostability for the perovskite solar cell were demonstrated, while creating highly saturated colors (i.e., red, green blue) with high Lightness. By focusing on red, green, and blue, we achieved remarkable PCE and long-term stability in perovskite solar cells, with only a 6%–10% reduction in PCE compared to noncolored references, alongside enhanced photostability and the creation of highly saturated colors with high Lightness. This is achieved through up to 45 layers and stack heights up to 5.3 μm, which might lead to increased costs and complexity in production. Further, the position of the layer stack and lack of texturing result in highly anisotropic color appearance with a clear Hue shift, which starts to appear between 20° and 30° viewing angle. A coloring technique for perovskite solar cells that combines all advantages—low PCE losses, high color saturation, high angular color stability, and the possibility of fast, large-area production—is highly desirable.

In this study, we combine perovskite solar-cell stacks with a commercially available MorphoColor[5] color filter on solar glass. We validate the angular resolved reflectance simulations based on wave optics and ray tracing with experimental data and analyze the color appearance from various viewing angles in terms of Hue, Chroma, and Lightness. We study the impact of individual layers on the color appearance and the maximum achievable short-circuit current density in the perovskite solar cell. By applying Bayesian optimization, we minimize the distance in color space to the targeted MorphoColor appearance. We particularly investigate how bridging layers between the MorphoColor color filter and the perovskite solar cell can be optimized with respect to the color impression and angular color stability. Finally, we present an optimized layer stack featuring both the desired color appearance as well as an increased photocurrent in the solar cell.

2. Optical Simulations and Validation

Figure 1 shows the layer stacks investigated in this work with the respective color-coded layers as described in **Table 1**. In this study, we consider the perovskite solar-cell layer stack as an integrated part of the color filter design.

All layer stacks used for the simulations have the same configuration from the top starting with an infinite layer of air, followed by an antireflective coating and a back-textured glass. Then, depending on the stack follows a perovskite solar cell (Figure 1a), a MorphoColor color filter (Figure 1b) or a combination of both with the perovskite solar cell deposited onto the color filter layers without any further adaptions (PEROMORPHO [PM], Figure 1c). The end of the stack is always an infinite layer of ethylene vinyl acetate (EVA) sheet, which is a thermoplastic polymer sheet that encapsulates solar cells. The outer infinite layers ensure that the results are not distorted by unwanted boundary effects.

The MorphoColor stack is composed of alternating silicon nitride (SiN) and titanium dioxide (TiO_2) layers and a silicon oxide (SiO_2) layer on top (MORPHO, Figure 1b). The solar-cell stack (PERO, Figure 1a) starts with an indium tin oxide layer (ITO, purple). The perovskite absorber is a double-cation/double-halide perovskite with a composition of $Cs_{0.2}FA_{0.8}Pb(Br_{0.1}I_{0.9})3$ and a bandgap of ≈1.68 eV. The perovskite layer is followed by 23 nm of fullerence (C_{60}) as electron-transport layer, 8 nm of bathocuproine (BCP) as buffer layer, and by 100 nm of silver as metal back contact. The self-assembled monolayer as hole-transport layer was omitted in the simulations due to its negligible influence on absorptance, as shown in ref. [18]. The perovskite solar-cell stack is based on ref. [19,20] and is used for perovskite/silicon tandem solar cells. Details on the fabrication of the perovskite solar-cell layer stack can be found in Section 5.1 and the characterization details in Section 5.2.

Figure 1d,f shows photographs of the three-layer stacks on a black background in white diffuse light with the same viewing conditions and the glass superstrate facing the camera. The brownish Hue of the perovskite (see Figure 1e) is often considered as aesthetically unappealing. Figure 1f shows the combined PM appearance without further adaptations. An undesired yellow stain can be observed compared to the clear green appearance of MORPHO. Figure 1g shows the SEM image of the PM stack with the respective layers colored.

The optical simulations for the MorphoColor layer stacks were performed with the MATLAB GenPro4 software,[21] which is an optical model for solar-cell simulations with ray tracing for surface textures and the net-radiation method. In the GenPro4 software, the user can choose the type of coupling, that is coherent and incoherent, for each layer. For crystalline-silicon-based PV modules, the color filter is optically separated from the solar cell due to a tall encapsulation layer. As a consequence, the propagation of light in between the MORPHO layer stack and the silicon solar cell is treated incoherently. In contrast to conventional silicon based solar modules, perovskite solar cells can be deposited directly on the PV cover glass. Consequently, the color filter and the solar cell form one stack where the light propagates coherently. As a further difference, the higher red/infrared reflectance of perovskite solar cells can require an adapted design. However,

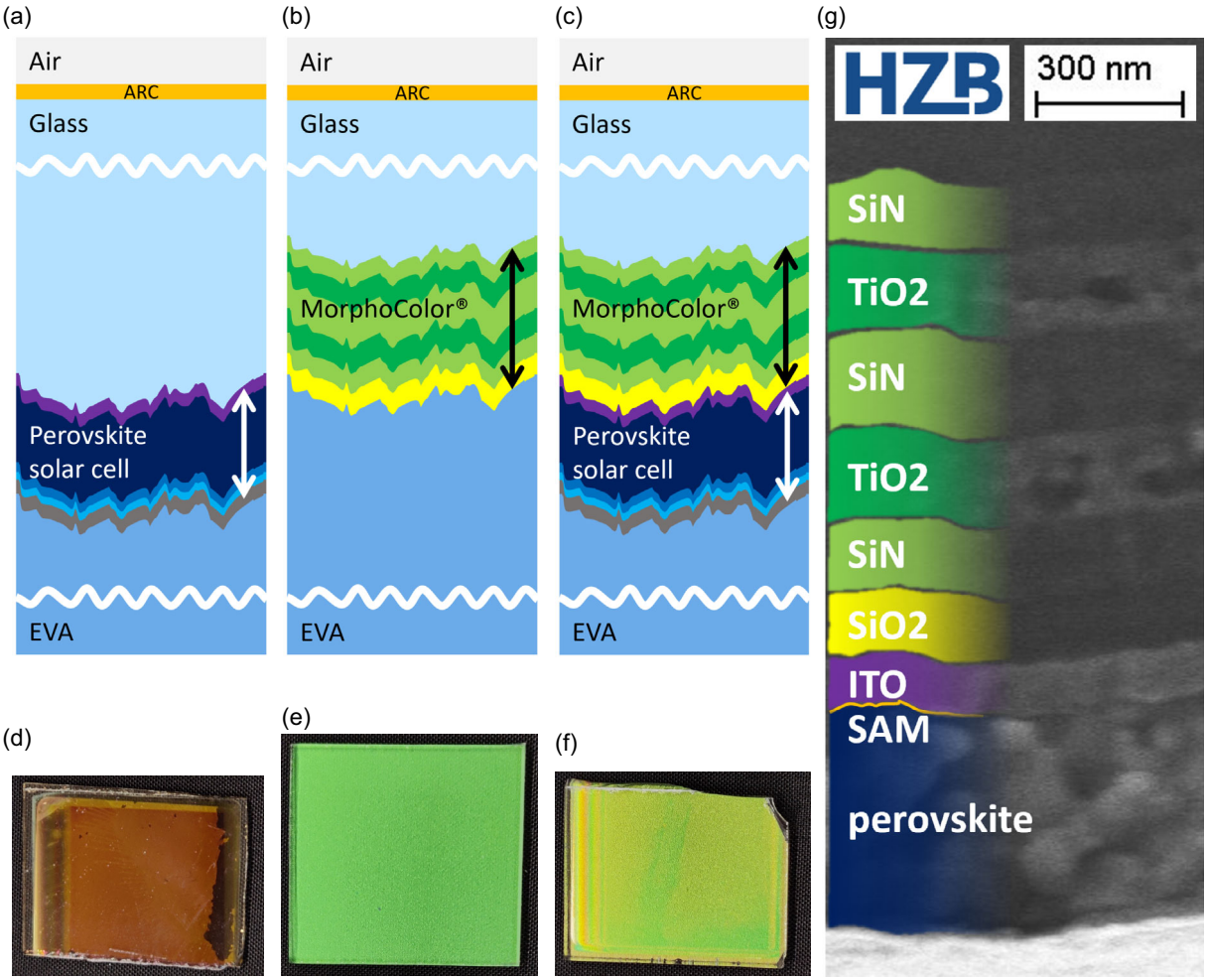

Figure 1. Layer stacks of a) a bare perovskite solar cell ("PERO"), b) a MorphoColor interference color layer stack ("MORPHO"), and c) a combination of both by subsequent deposition ("PEROMORPHO"). d–f) Photographs of the three-layer stacks on black background in the same viewing conditions of white diffuse light with the glass superstrate facing the camera. g) An scanning electron microscope (SEM) image of a PEROMORPHO layer stack.

the perovskite investigated in this study does not feature an enhanced red reflectance. **Figure 2**a shows the schematics of the light paths in the simulation. Light impinges from one incidence interval, i.e., a solid angle range, and is reflected back into all intervals of the space with respective reflectance values. More details on optical simulations can be found in Section 5.3.

In the following, the simulated reflectance at the light path directions is compared to the respective hemispherically integrated reflectance measurements in Figure 2c,d.[22] Figure 2c shows the simulation and experimental results of the MorphoColor stack in position 1 (terminology used in glazing industry which numerates the interfaces, i.e., air–MorphoColor–glass). The MORPHO stack is on the front side of the structured glass and light is incident from above; thus, the light interacts with the MorphoColor stack without traveling through the glass first. The measurement procedure and data were published in ref. [9]. The simulated reflectance follows the experimentally obtained reflectance curve closely. The alignment of the characteristic peak (between 500 and 550 nm) matches closely for viewing angles 8° and 60° but deviates slightly to smaller and larger wavelengths for 40° and 20°, respectively. The minima of the simulated curves at shorter wavelengths are slightly underestimated with respect to measured quantities. The mean bias error (MBE) is 0.006, the root mean square error (RMSE) is 0.022, and the mean absolute error (MAE) is 0.016 for all angle of incidence (AOI) combined.

The results for the MORPHO stack layout (position 2, i.e., air–glass–MorphoColor) are shown in Figure 2d; the experimental data was obtained by in-house measurements and also compared to its simulated pendant. Figure 2b shows the schematics of the apparatus. The characterization procedure for the measurements is described in Section 5.2. The results show very good agreement of simulation and measurement for the peak positions. The MBE is 0.001, the RMSE is 0.022, and the MAE is 0.016 for all AOIs combined. The global maxima are slightly overestimated. This observation can be traced back to the model for the layer thickness. The interference behavior depends on the angle of incidence, which varies locally for a textured surface. The superposition of all local reflectance spectra results in less pronounced minima and maxima due to the phase shift induced by

Table 1. Layer stack of PEROMORPHO structure (see Figure 1c) as used for simulations.

Object	Description		Color	Height [nm]	Geometry	Coherence
Layer	Air			inf	Non-conformal	Incoherent
Coating	ARC			100	Conformal	Coherent
Layer	Glass			1.1e6	Non-conformal	Incoherent
Texture	- - - -		- - - -	- - - -	- - - -	Coherent
Coatings	Color Filter	SiN_2		142	Conformal	
		TiO_2		164.5		
		SiN_2		203		
		TiO_2		164.5		
		SiN_2		142		
		SiO_2		160		
	Solar Cell	ITO		110		
		Perovskite		550		
		C_{60}		23		
		BCP		8		
		Ag		100		
Layer	EVA			inf	Non-conformal	Incoherent

inclined surfaces. This effect is combined with the conformal texture geometry model, which designs layer thicknesses normal to the local surface following a cosine relation. The texture is simulated on the basis of a surface profile measurement. This effective thickness relation for incidence light under large AOIs is overestimated since the realistic layer growth is a combination of directed and isotrope growth behavior. The flanks of the steeper structures are thus effectively thinner than in reality which leads to stronger blueshifts of the local reflectance compared to the planar surface. Taken together, these effects lead to lower minima and maxima of the reflectance. The bulk glass layer induces multiple interactions which result in various angle of incidences and multiple wavelengths for the constructive interference. As a consequence, the main peak is reduced in height compared to the simulation, which overestimates the peak height and underestimates the complexity of the multiple interactions.

3. Color Optimization

As shown in Section 2, perovskite solar-cell stacks combined with an unadapted MorphoColor filter do not exhibit the same bright green color as the bare MorphoColor stack 1b. Therefore, we performed optical simulations to optimize the color impression of the perovskite solar cells. For this optimization, we first need to define various color spaces and transformations. Appendix A1 provides formulas based on the definitions of the International Commission on Illumination (CIE).[23] The reflectance spectrum $R(\lambda)$ is weighted with the CIE 1931 *XYZ* color-matching functions (CMFs) and the D65 illuminant to obtain the CIE *XYZ* color coordinates, comparing Equation (A1)–(A4). The D65 illuminant represents standard daylight conditions. These coordinates are then transformed to CIE LCh coordinates for color appearance study, following ref. [6]. The CIE Lab and its cylindrical version, CIE LCh_{ab}, describe color Lightness L, Chroma C, and Hue h. The CIE ΔE^*_{00} measure quantifies color differences in just noticeable differences (JND) and is defined in the CIE Lab color space, with its main formula in Equation (1). For more details, see ref. [24].

$$\Delta E^*_{00} = \sqrt{\left(\frac{\Delta L'}{k_L S_L}\right)^2 + \left(\frac{\Delta C'}{k_C S_C}\right)^2 + \left(\frac{\Delta H'}{k_H S_H}\right)^2 + R_T \frac{\Delta C'}{k_C S_C}\frac{\Delta H'}{k_H S_H}} \tag{1}$$

$\Delta L'$, $\Delta C'$, and $\Delta H'$ are the differences in Luminance, Chroma, and Hue obtained from two colors in CIE Lab space; S_L, S_C, and S_H are correct nonuniformities in CIE Lab; and k_L, k_C, and k_H are correct differences in color perception due to illumination. Finally, R_T mainly corrects the Hue and Chroma values in the blue region. To display the color appearances on monitors, printers, and Internet, the sRGB color space is used. These transformations described earlier are implemented in the publicly available Python library Colour Science.[25]

The optimization of the stack design is performed with a Bayesian optimization method based on Gaussian process surrogate models,[26] in a commercial implementation by JCMwave GmbH. Bayesian optimization is especially suited for this task due to the expensive forward problem (runtime about 3 min on server), its ability to optimize for a global solution and handle complex problems with fewer evaluations. The details of this optimization strategy will be described elsewhere.[27] In short, Bayesian optimization constructs a statistical model for the objective function (Equation (2)). The model predictions are used to determine promising parameter samples that maximize, for example, the expected improvement over the best design seen so far. Since the statistical model, typically a Gaussian process, takes all previous function evaluations into account, Bayesian optimization requires generally fewer

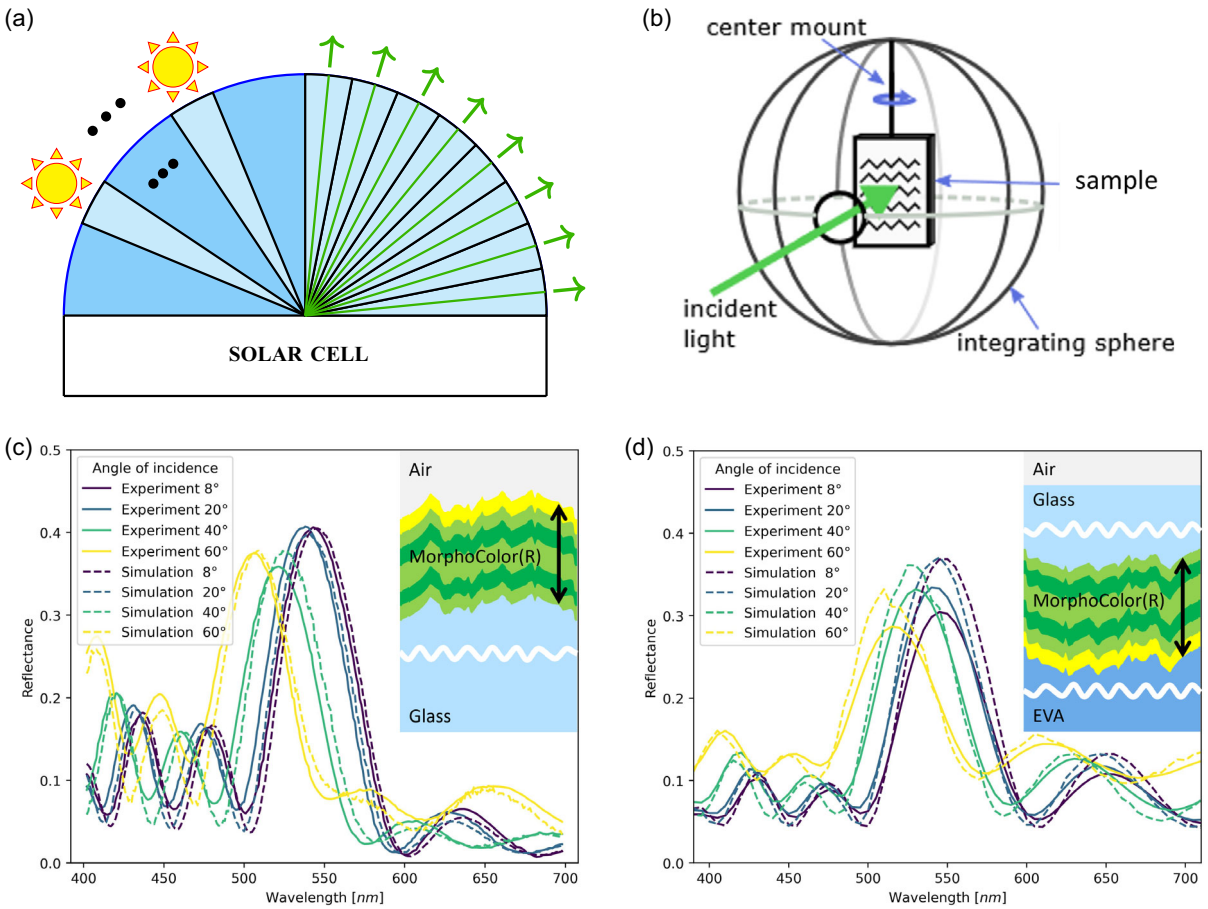

Figure 2. VALIDATION OF SIMULATIONS WITH REFLECTANCE MEASUREMENTS: a) Experimental setup of angle-resolved reflectance measurement inside an integrating sphere using a rotatable center mount. b) Simulation setup for angular intensity distribution with incidence light interval.[22] c) Measured hemispherically integrated reflectance spectra of MorphoColor from ref. [9] and data simulated with GenPro4 at incidence angles of 8°, 20°, 40°, and 60°. Layer stack shown on the right is on the front side of the structured glass (position 1) and light comes from above. Here, simulation and experiment overlap and show only small deviations, i.e., the main peak of 40° and the dips from 400 to 500 nm. d) Same as (c) but the layer stack is on the backside of the structured glass (position 2) and light comes from above. This layout is referred to as MORPHO, as shown in Figure 1b. Simulation and experiment overlap and show only small deviations, i.e., the main peaks are overestimated and the dips slightly underestimated.

evaluations than many heuristic global optimization methods.[27] The training of a Gaussian process with evaluations of the scalar objective value D hides information about the composition of the objective in terms of Lightness, Chroma, and Hue mismatches. Therefore, we train a set of Gaussian processes directly on the values $\Delta L'$, S_L, $\Delta C'$, S_C, $\Delta H'$, S_H, and R_T for each angle θ_i. Their prediction is then used to determine more accurate values of the expected improvement and to further decrease the number of required evaluations to find good designs.

Equation (2) shows the objective function for this optimization, which is the sum over the color–distance measure described in Equation (1) for two different color-filter stacks and a group of viewing angles. This color distance measure is based on the CIE uniform color space Lab and is widely used for color filter design.[5,8] The color distances are calculated for the reference, that is, only the simulated MorphoColor color filter, referenced as MORPHO in Figure 1b, and the new proposed color filter stack for a group of incidence angles. A cosine weighting factor was introduced to reduce the influence of large incidence angles, which can be suppressed due to their low Chroma and high Lightness trend. The objective is to minimize the cosine-weighted and angle-averaged perception distance D.

$$D = \sum_i \cos(\theta_i) \cdot \Delta E^*_{00,i}(\mathrm{Lab}_{\mathrm{ref},i}, \mathrm{Lab}_{\mathrm{ref},i}) \tag{2}$$

with θ_i the angle of incidence. **Figure 3** illustrates the steps for determining the objective in each iteration of the optimization. The GenPro4 simulation is started for a set of layer parameter samples and for a set of viewing angles. Figure 3a shows isotropic illumination conditions with varying viewing angles dependent on the angular binning of the simulation. While the figure shows only eight bins, the number in the simulation was 90 with 1° step size. For each simulation, first the reflectance spectrum (Figure 3b, upper) is translated to CIE XYZ via the CMFs (Figure 3b, lower) and further to CIE Lab and CIE LCh (Figure 3c). The objective function is evaluated with the results and the process begins from the start again.

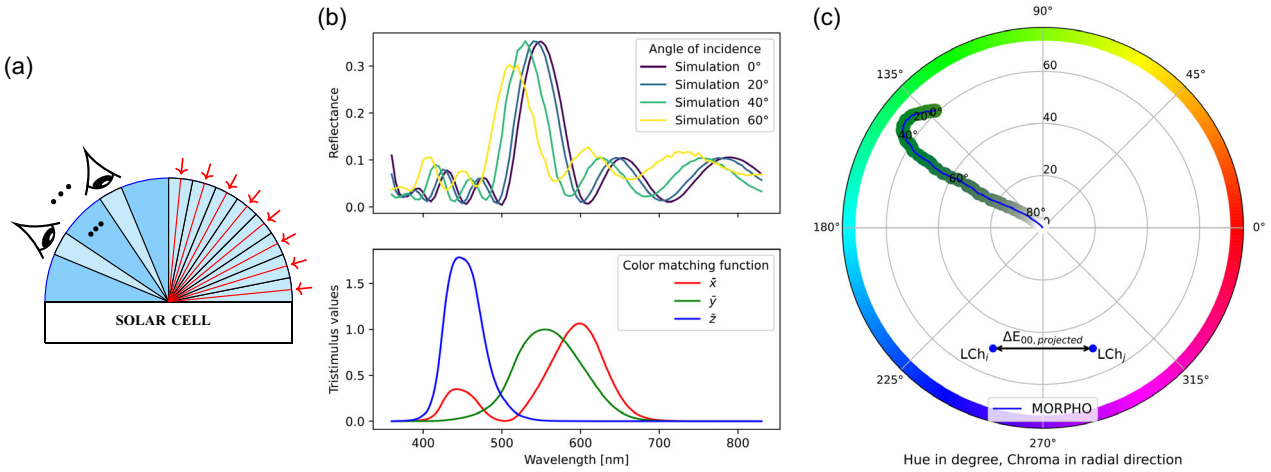

Figure 3. DETERMINATION OF THE OBJECTIVE FUNCTION: a) Schematics of isotropic illumination conditions and varying angles of observation (AOO) and b) (upper) their reflectance spectra and (lower) CIE 1931 color-matching functions (CMFs) which are based on the optical response curves of the human eye. The weighted integral of both curves in (b) and further transformations result in color coordinates with dimensions Lightness, Chroma, and Hue. c) The Hue and Chroma representation over the course of 90° AOO. Further, the projected ΔE^*_{00} color distance metric measuring the distance between two points in this color space is depicted.

Figure 4 shows the result of the optimization process. This was selected after two separate optimization runs with 100 iterations each. The optimized stack layout is shown in Figure 4a and the respective layer heights in Figure 4b. The reflectance of the combined PM stack was simulated to estimate its color appearance. Figure 4c shows tiles with the estimated color appearance of four different stacks, i.e., PERO, MORPHO, PM as described in section Figure 1 and the "PEROMORPHO optimized" stack as shown in 4a. The color appearance of PM varies greatly from the MORPHO benchmark case. The color appears brighter, but for viewing angles close to the surface normal (5°–30°), it appears tinted brown. Figure 4d,e validates these observations, since the Lightness values are higher for the PM case than for MORPHO or PERO. Further, while the Chroma values are just slightly smaller for PM, a noticeable Hue shift is observable. With increasing viewing angles, all tiles become less saturated and brighter. In Figure 4d,e, the respective Lightness, Hue, and Chroma values are shown. The higher overall reflectance at high angles of observation (AOO) results in less pronounced reflectance peaks of the designed color. This leads to reduced Chroma and higher Lightness values, while the Hue remains stable.

To obtain a color appearance close to the original MorphoColor, the following optimization was performed. The thicknesses of the final two layers in the color filter (SiN_2, SiO_2) were allowed to vary between 0 and 300 nm. The upper bound was chosen around 50% larger than the previous highest layer thickness and the lower bound so that omitting a layer is possible. The constraint has the purpose of reducing the parameter space and thus enhancing the convergence to the minimum. The choice to optimize only the last two layer thicknesses is based on the estimation that the ITO layer has a similar refractive index in the range from 400 to 700 nm as SiN_2. As a consequence, the ITO layer can be integrated into the color filter and the SiO_2 layer can be omitted. Figure 4c shows the color impression for the four different stack layouts. Their respective coordinates in CIE LCh space are shown in Figure 4d,e. The perovskite stack has a grayish appearance with low Lightness and Chroma. The difference in color appearance to 1d is due to the deterioration of the perovskite, which leads a Hue shift. Combined with the original MorphoColor stack, the appearance starts from a muted green–brownish color and shifts to a bright green for larger AOO. The result of the "PEROMORPHO optimized" stack is close to the MORPHO stack's color appearance. The chosen candidate from the optimization process differs from the color filter as shown in Table 1 as estimated. The thickness of the lowest SiN_2 was reduced from 142 to 91 nm, whereas the neighboring SiO_2 layer vanished completely (0 nm). Although the Lightness values are slightly lower by 2–3 JND, the Chroma and Hue angles overlap. This results in a slightly lower Lightness but very similar color appearance. We explain these findings as follows: a standalone MorphoColor color filter with air or a laminate (e.g., EVA) with a respectively large layer height adjoining the color filter is considered a case of incoherent light coupling, where the closing SiO_2 layer of the filter has an antireflective effect. In contrast, for a combined layer system, i.e., the color filter on glass combined with a perovskite solar-cell layer stack, coherent light coupling has to be taken into account. In this case, the bridging layer SiO_2 is found to have a detrimental effect to the designed color appearance and was omitted. In addition, the optical similarities of the now neighboring SiN_2 layer of the color filter and the ITO layer of the perovskite solar cell enable a reduction of the respective SiN_2 layer height for optimum color appearance. The GenPro4 software estimates the photoinduced current density in the absorbing perovskite layer for the PERO stack with $J_{ph} = 20.5\ mA\ cm^{-2}$. The PM stack reaches $J_{ph} = 18.5\ mA\ cm^{-2}$ and the "PEROMORPHO optimized" stack $J_{ph} = 19.6\ mA\ cm^{-2}$. In relation to the PERO case without color filter, 90% and 96% are achieved, respectively. Since the Lightness and Chroma quantities have a quasi-linear relation with the relative loss, as shown

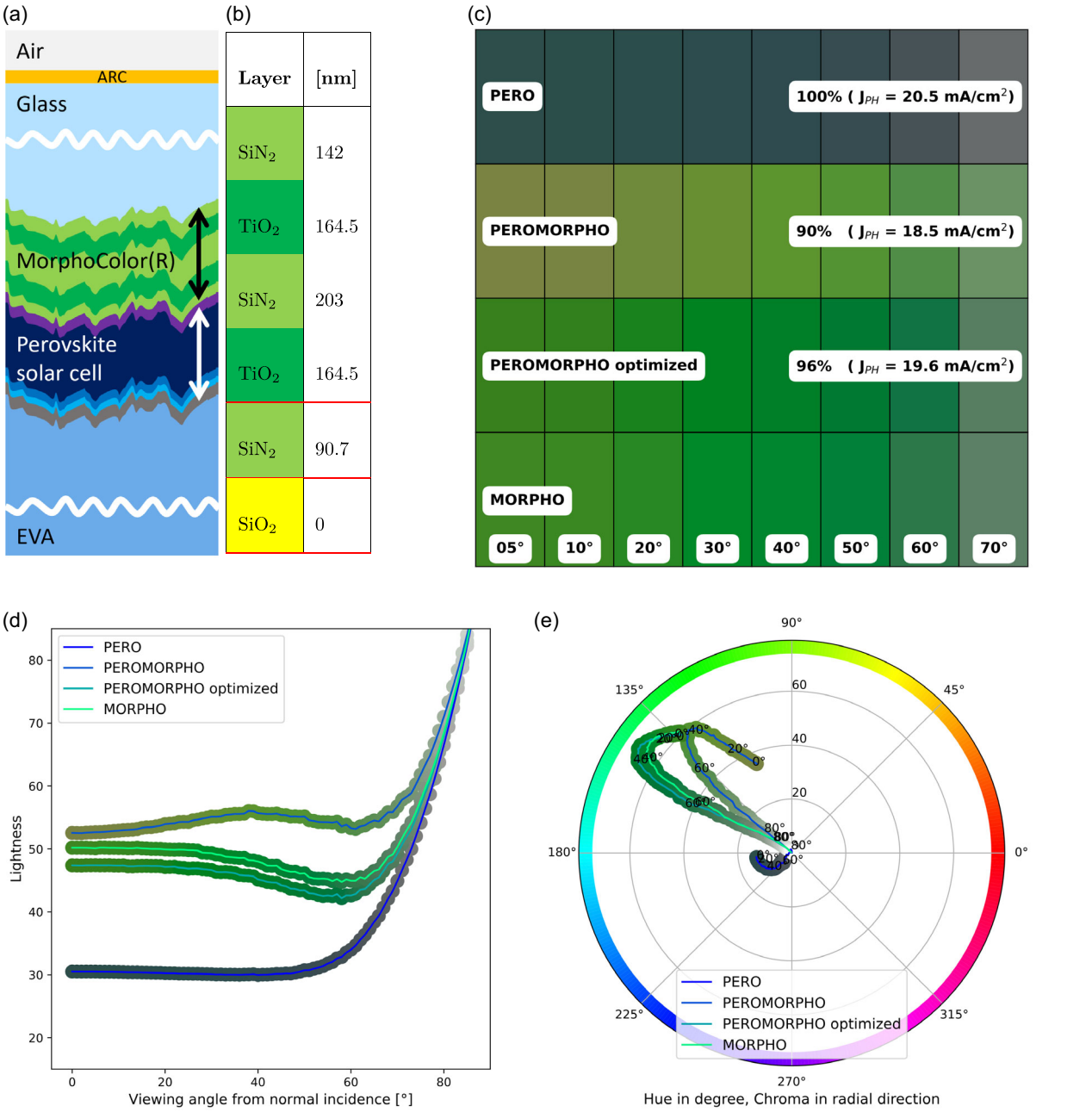

Figure 4. OPTIMIZATION RESULTS: a) final stack "PEROMORPHO optimized" and b) its layers of the color filter. c) Color impression, d) Lightness, and e) Chroma and Hue for four different stack designs (perovskite solar-cell PERO, perovskite solar cell on unchanged MorphoColor PEROMORPHO, perovskite solar cell on MorphoColor inspired color filter "PEROMORPHO optimized" and unchanged MorphoColor color filter on its own MORPHO). Each color impression is shown for various viewing angles from the surface normal.

in ref. [6], this behavior was expected and can be explained this way. The objective function is thus considering the photoinduced current density of the solar cell through the Chroma and Lightness values of the CIE $\Delta E^*_{00,i}$ metric. Further investigation of the objective function definition is necessary with regard to maximizing the current while minimizing the color difference.

We fabricated samples with the optimized layer stack geometry according to the outcome of the numerical simulation results as shown in Figure 4b, and with perovskite solar-cell layer stacks except the rear reflector. As the perovskite absorber layer of these experimental samples was with ≈400 nm thinner then designed leading to a reduced absorption of red light, we decided to replace the rear reflector by a black light trap in the optical measurements. **Figure 5** shows a comparison of the simulated results and experimental data. PERO, PM, and "PEROMORPHO optimized" samples are shown in a photograph in Figure 5a

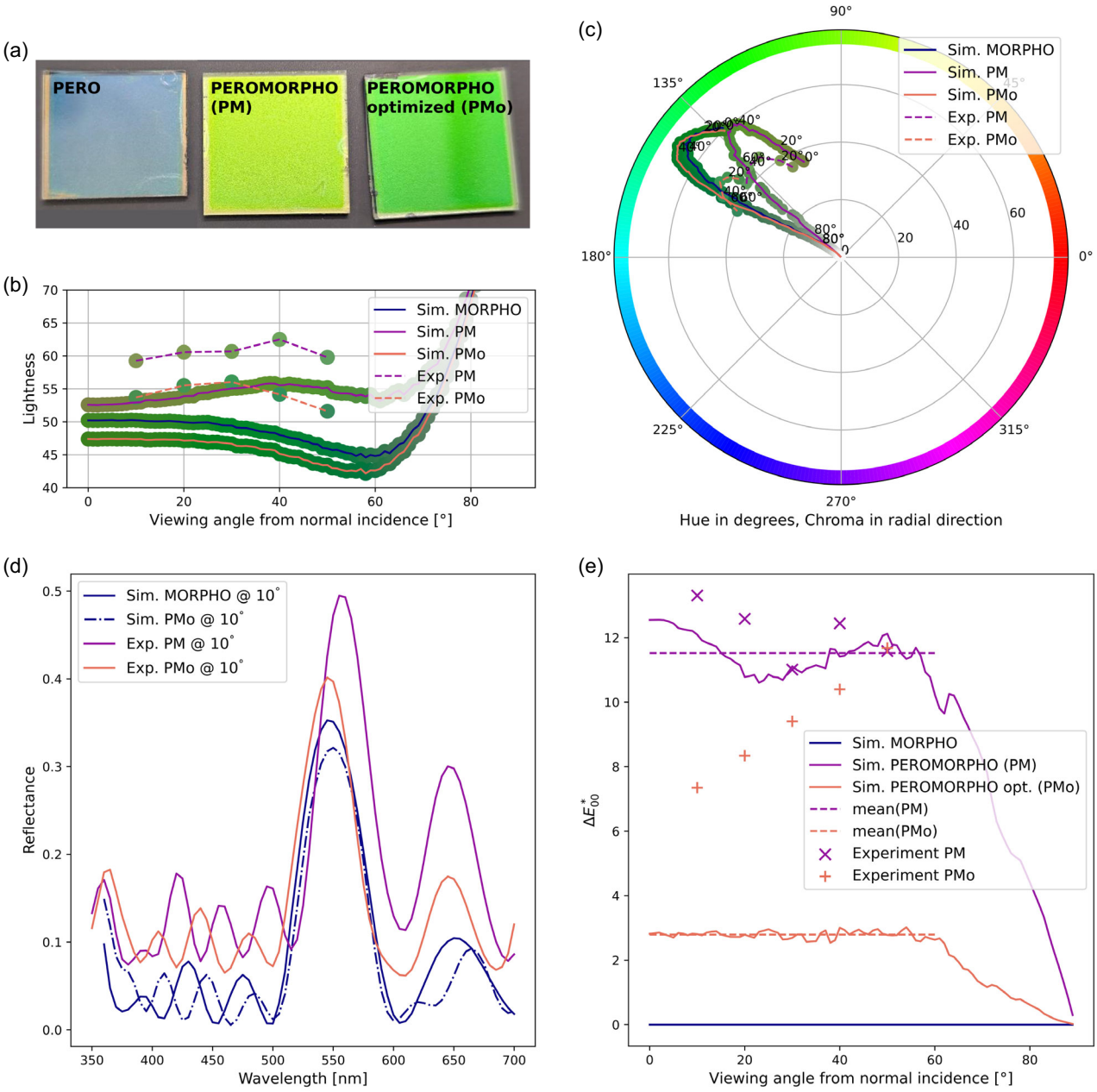

Figure 5. EXPERIMENTAL RESULTS: a) photographs of samples PERO, PEROMORPHO (PM), and "PEROMORPHO optimized" (PMo) in the same viewing conditions of white diffuse light with the glass superstrate facing the camera; b) Lightness and c) Hue and Chroma for simulated MORPHO, PM, and PMo for all viewing angles, and experimental data of PM and PMo from 10° to 50° in 10° steps; d) reflectance comparison of simulated MORPHO and PMo with experimental PM and PMo spectra at 10° AOO; and e) ΔE^*_{00} comparison of simulated MORPHO to simulated PM and PMo, including experimental data.

and show a clear difference between PM and "PEROMORPHO optimized". While the non-optimized version of PM has a yellow tinted color appearance compared to the bare MORPHO as shown in Figure 1e, "PEROMORPHO optimized" has the desired green appearance. The quantitative results of the color analysis are shown in form of a Lightness comparison in Figure 5b and a Hue and Chroma comparison in Figure 5c. Both measured Lightness curves are higher than in the simulations. The contrary is observed for the Chroma. The arcs of the experimental data clearly show the designed Hue shift between PM and "PEROMORPHO optimized". Figure 5d shows the respective reflectance spectra measured and simulated at 10° AOO. The main peak position at ≈550 nm is well met in the experimental samples. A major difference between PM and "PEROMORPHO optimized" can be observed concerning the side peak at ≈650 nm. In both, experiments and simulations, this side peak could be reduced by using the optimized stack. Deviations between experimental and numerical results

concerning Lightness and Chroma might stem from the deviations in perovskite layer thickness and the missing remaining rear reflector layers (C_{60}, BCP, and Ag). However, the beneficial impact of the optimization on Hue is experimentally clearly shown.

Figure 5e compares the original MORPHO configuration with both the simulated and experimental PM and "PEROMORPHO optimized" data via the $\Delta E^*_{00,i}$ metric, which includes all three previously discussed properties Hue, Chroma, and Lightness. PM reaches for AOO 1°–60° an average distance of $\Delta E^*_{00,i} = 11.5$ in the simulations. In contrast, the simulated "PEROMORPHO optimized" reaches for AOO 1°–60° an average distance of $\Delta E^*_{00,i} = 2.8$. From AOO 60°–90°, both $\Delta E^*_{00,i}$ values approach zero. The respective experimental values extracted from reflectance spectra exhibit higher values, which can be attributed to the deviations in Chroma and Lightness. But also here, the values for the "PEROMORPHO optimized" case are substantially smaller than in the non-optimized case. The reflectance plots and respective layer stacks are shown in Appendix A3.

4. Conclusion

We successfully adapted a MorphoColor color filter, which was initially designed for use with silicon solar cells, to be compatible with perovskite solar cells. By combining optical simulations and Bayesian optimization techniques we adapted the bridging layers between color filter and perovskite solar cell such that the achieved color appearance matches closely the original appearance. In numbers, for the angles of observation from 1° to 60°, the difference in color space $\Delta E^*_{00,i}$ reduces from around 11.5–2.8 after optimization. For larger angles of observation from 60° to 90°, the difference $\Delta E^*_{00,i}$ approaches zero. We validated the numerical results by fabricating color filters featuring the layer stack geometry resulting from the numerical optimization and combining them with a perovskite solar-cell layer stack. These optimized layer stacks show a color impression in terms of Hue much closer to the original MorphoColor color filter than the respective layer stacks without optimization. Further, the optimizations allowed to reduce the relative photocurrent density loss in the perovskite absorber layer induced by the color filter from 10% to 4% showing the potential of including the perovskite solar cell as a functional part of the color filter design. The design approach with net-radiation method, ray tracing, and Bayesian optimization is promising for further simulations, e.g., other textures, materials, and various color aims. The optimization method presented in this manuscript can be applied to all thin-film solar module designs, where the solar-cell stack is directly deposited onto a glass substrate. Future work could be the fabrication of the designed colorful perovskite solar cells with a closely controlled fabrication of the designed layers. A next step could include enhancement of the optimization method to choose between a set of materials with different refractive index values for each layer. This would generalize the optimizers' ability to freely inverse design color filters. Further steps could focus on number of color filter layers and constraints about maximum total layer thickness or minimum efficiency loss. Improvements would further reduce manufacturing costs and boost energy yield.

5. Numerical and Experimental Methods

5.1. Device Fabrication

To fabricate the PM stack, 100 nm ITO were deposited on MorphoColor by radio-frequency sputtering of a ceramic target in argon/oxygen sputter gas mixture, with an oxygen concentration of 0.2%. For the planar reference, glass with patterned ITO substrates was used. Then, [2-(9H-carbazol-9-yl)ethyl]phosphonic acid 2PACz was spin-coated at 3000 rpm for 30 s onto the substrates and annealed at 100 °C for 7 min in a nitrogen-filled glove box. $Cs_{0.2}FA_{0.8}Pb(Br_{0.1}I_{0.9})3$ perovskite layer (composition estimated from rates) was evaporated using a CreaPhys PEROvap tool in an nitrogen glove box with a base pressure of 2×10^{-6} mbar and a shielding temperature of –25 °C surrounding the evaporation sources. Deposition lasted for 94 min. The substrates were then annealed at 180 °C for 5 min in nitrogen-filled glove box. And, 18 nm of fullerence (C_60) from ChreaPhys GmbH was used as electron-transport layer, and 8 nm of BCP from Sigma Aldrich was used as buffer layer. Both were then deposited via thermal evaporation in base pressure of 1×10^{-6} mbar. And, 100 nm of Ag were then evaporated as a metal contact.

5.2. Characterization

Angle-resolved reflectance measurements were conducted with a UV/visible/near-infrared spectrophotometer (Lambda 1050+, Perkin Elmer). The spectra were acquired using a center mount sample holder, enabling center-axis rotation of samples within an integrating sphere. Measurements started at 5° and 8° and then continued in 10° increments from 10° to 70°. Each spectrum was recorded in 5 nm increments ranging from 300 to 1300 nm. Prior to measurement, adhesive black absorber sheets were attached to the MorphoColor glasses using an index matching liquid (IML 150, Norland). This configuration enables capturing the front-side reflection characteristics without interference from the backside interface. The backside of the absorber sheet was attached with a white cleanroom cloth to minimize its absorption within the integrating sphere.

5.3. Optical Simulations

The simulations were performed with the MATLAB GenPro4 software,[21] which implements the net-radiation method with ray tracing for solar-cell simulation. GenPro4 can be set to differentiate between two approaches depending on the material thickness in comparison to the coherence length of sunlight (≈1 μm). Thin coherent "coatings" account for interference while incoherent "layers" do not. GenPro4 can simulate fully 3D textures with ray tracing but projects them into 2D angular intervals. While coatings are treated conformally, i.e., with the same texture on the front- and backside, layers can have different textures on their interfaces and are thus treated nonconformally. The simulated reflectance of a configuration is obtained and an example is shown in Figure 3b. Following Equation (3), the photoinduced current density J_{ph} is estimated, which itself equals approximately the short-circuit current density J_{sc}, if the series resistance is omitted and the charge carrier diffusion length is assumed infinite. With λ_g as the bandgap wavelength of the perovskite, λ_{min} the

minimum wavelength of the simulation, $A_{\text{pero}}(\lambda)$ as the absorption in the perovskite layer, and $I(\lambda)$ as the AM1.5G standard solar irradiance spectrum, the photoinduced current density is

$$J_{\text{ph}} = \int_{\lambda_{\text{min}}}^{\lambda_{\text{g}}} \frac{q\lambda}{hc} A_{\text{pero}}(\lambda) I(\lambda) \text{IQE}(\lambda) \text{d}\lambda \tag{3}$$

The reciprocity assumption was introduced since the simulation of the inverted light path case, i.e., using the simulations with light coming from one AOI direction (forward, Figure 2a) as the AOO under diffuse illumination conditions (backward, Figure 3b), did not obtain physically reasonable results. This was stated in ref. [21] and is reproduced in this study. The origin of the lack of reciprocity is assumed to be caused by the small-texture model in combination with the 3D to 2D mapping, which works well for the forward direction but is incomplete for this backward case. This possible explanation is based on the observation, that introducing a textured surface strongly increases this effect. **Figure A1** shows the forward and backward reflectance spectra for a planar and a textured simulation.

Appendix

CMFs

Equation (A1)–(A4) with Equation (A4) form the *XYZ* tristimulus values of the CIE *XYZ* color space. Hereby, the $\overline{x}(\lambda)$, $\overline{y}(\lambda)$, and $\overline{z}(\lambda)$ CMF is weighted by the reflectance $R(\lambda)$ and the illuminant $S(\lambda)$. We used the D65 illuminant spectrum (W m^{-3}) defined by CIE and represents daylight conditions and the CIE 1931 2° observer CMFs as shown in the bottom plot of Figure 3b.

$$X = K \int_{360\,\text{nm}}^{830\,\text{nm}} R(\lambda) S(\lambda) \overline{x}(\lambda) \text{d}\lambda \tag{A1}$$

$$Y = K \int_{360\,\text{nm}}^{830\,\text{nm}} R(\lambda) S(\lambda) \overline{y}(\lambda) \text{d}\lambda \tag{A2}$$

$$Z = K \int_{360\,\text{nm}}^{830\,\text{nm}} R(\lambda) S(\lambda) \overline{z}(\lambda) \text{d}\lambda \tag{A3}$$

$$K = \frac{1}{\int_{360\,\text{nm}}^{830\,\text{nm}} S(\lambda) \overline{y}(\lambda) \text{d}\lambda} \tag{A4}$$

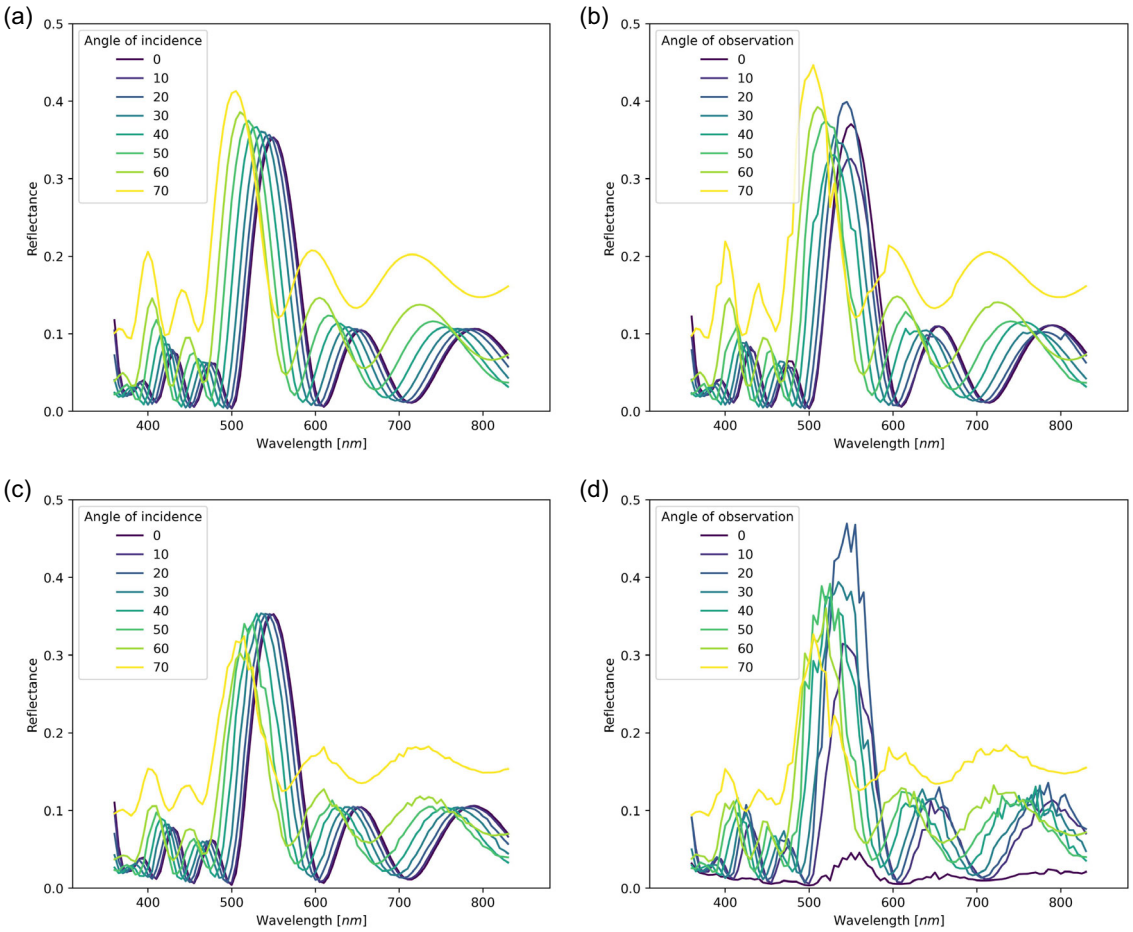

Figure A1. REPRODUCED LACK OF RECIPROCITY IN GenPro4: a,b) The angle of incidence (forward) and angle of observation (backward) direction for the planar, not textured case. c,d) The textured case. In all cases, model "ray" was chosen with either a flat profile for the planar case or a textured profile for the textured case.

GenPro4: No Reciprocity for Small-Textured Surfaces

Figure A1 shows the reproduction of the lack of reciprocity for textured surfaces in the GenPro4 model as mentioned in ref. [21]. Four reflectance plots are shown with either texture/planar and a forward/backward direction. Physically reasonable forward solutions are compared to the backward solutions, which show diverging reflectance amplitudes. In addition to less smooth curves, the peak positions and shapes are comparable to the forward solutions.

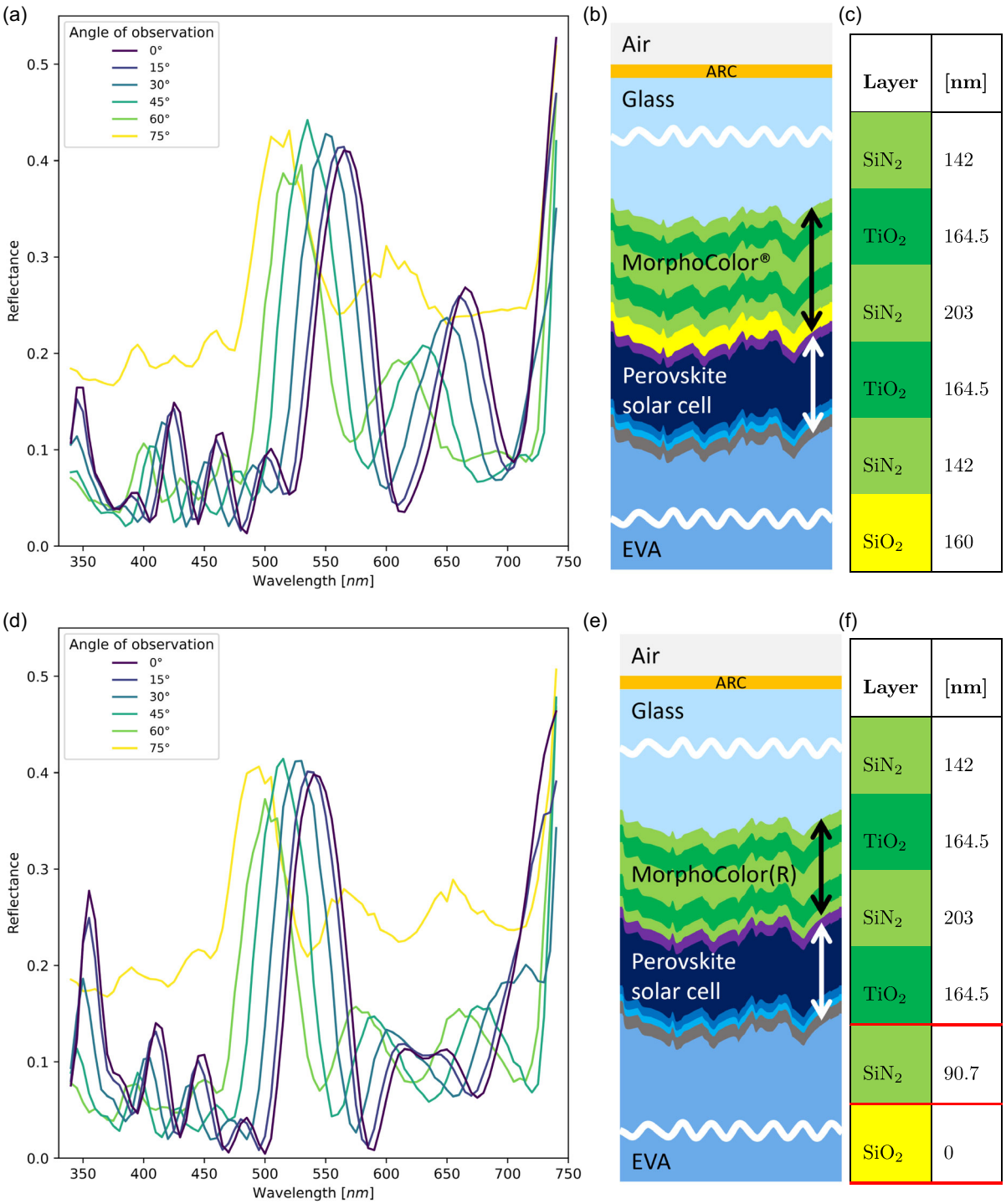

Figure A2. Simulated hemispherically integrated reflectance spectra for PEROMORPHO and PEROMORPHO optimized stacks. a) PEROMORPHO reflectance; b) stack; c) layer; d) PEROMORPHO optimized reflectance; e) optimized stack; and f) layers.

Results: PM and PM Optimized

Figure A2 shows the details of PM and optimized PM, their stack layouts and reflectance curves. The red framed rows in Figure A2 (f) show the changed layer heights.

Supporting Information

Supporting Information is available from the Wiley Online Library or from the author.

Acknowledgements

J.S. thanks the Helmholtz Einstein International Berlin Research School in Data Science (HEIBRiDS) for funding. The results were obtained at the Berlin Joint Lab for Optical Simulations for Energy Research (BerOSE) of Helmholtz-Zentrum Berlin für Materialien und Energie, Zuse Institute Berlin, and Freie Universität Berlin.

Conflict of Interest

The authors declare no conflict of interest.

Author Contributions

Jonas Schaible: conceptualization (equal); data curation (lead); formal analysis (lead); investigation (lead); methodology (equal); project administration (equal); software (lead); validation (equal); visualization (lead); writing—original draft (lead); and writing—review and editing (equal). **Hanifah Winarto**: data curation (lead); investigation (supporting); and writing—original draft (supporting). **Viktor Škorjanc**: data curation (equal) and formal analysis (equal). **Ivan Sekulic**: methodology (equal); software (equal); and writing—original draft (supporting). **Philipp-Immanuel Schneider**: methodology (equal); software (equal); and writing—original draft (supporting). **Danbi Yoo**: data curation (equal); methodology (equal); and writing—original draft (supporting). **Lea Zimmermann**: data curation (equal) and writing—original draft (supporting). **Andreas Wessels**: data curation (equal); formal analysis (supporting); investigation (supporting); resources (equal); and writing—original draft (supporting). **Benedikt Bläsi**: formal analysis (supporting); methodology (equal); supervision (supporting); and writing—original draft (equal). **Sven Burger**: formal analysis (supporting); funding acquisition (equal); methodology (supporting); project administration (equal); resources (equal); supervision (equal); and writing—original draft (equal). **Klaus Jäger**: conceptualization (equal); formal analysis (equal); funding acquisition (equal); methodology (equal); project administration (equal); software (supporting); and writing—original draft (equal). **Christiane Becker**: conceptualization (equal); funding acquisition (lead); project administration (equal); supervision (lead); validation (equal); and writing—original draft (equal).

Data Availability Statement

The data that support the findings of this study are available from the corresponding author upon reasonable request.

Keywords

Bayesian optimizations, building-integrated photovoltaics, color filters, colorful perovskite solar cells, MorphoColor

Received: August 28, 2024
Revised: November 6, 2024
Published online:

[1] Y. Li, L. Li, W. Deng, D. Zhu, L. Hong, *Buildings* **2023**, *13*, 389.
[2] P. Bonomo, F. Frontini, *Buildings* **2024**, *14*, 1510.
[3] A. B. Block, J. E. Palou, M. Courtant, A. Virtuani, G. Cattaneo, M. Roten, H.-Y. Li, M. Despeisse, A. Hessler-Wyser, U. Desai, A. Faes, C. Ballif, *Energy Build.* **2024**, *314*, 114253.
[4] C. Kutter, B. Bläsi, H. R. Wilson, T. Kroyer, M. Mittag, O. Höhn, M. Heinrich, in *35th European Photovoltaic Solar Energy Conf. and Exhibition*, Brussels, Belgium **2018**, Vol. *1488–1492*, 5 pages.
[5] B. Bläsi, T. Kroyer, T. Kroyer, T. Kuhn, T. E. Kuhn, O. Hohn, *IEEE J. Photovoltaics* **2021**, *11*, 1305.
[6] A. Royset, T. Kolås, O. Nordseth, C. C. You, *Energy Build.* **2023**, *298*, 113517.
[7] J. C. O. Lizcano, P. Procel, A. Calcabrini, G. Yang, A. Ingenito, R. Santbergen, M. Zeman, O. Isabella, *Prog. Photovoltaics* **2021**, *30*, 401.
[8] J. Lizcano, S. Villa, Y. Zhou, G. Frantzi, K. Vattis, A. Calcabrini, G. Yang, M. Zeman, O. Isabella, *Sol. RRL* **2023**, *7*.
[9] A. Wessels, A. Callies, B. Blasi, T. Kroyer, O. Hohn, *Opt. Express* **2022**, *30*, 14586.
[10] A. Wessels, L. Christen, A. Callies, T. Kroyer, O. Hoehn, B. Bläsi, *Opt. Express* **2023**, *31*, 20102.
[11] J. Halme, P. Makinen, *Energy Environ. Sci.* **2019**, *12*, 1274.
[12] P. M. Pearce, *Environ. Sci.* **2024**, *17*, 1189.
[13] Q. Jin, Q. Zhang, C. Rainer, H. Hu, J. Chen, T. Gehring, J. Dycke, R. Singh, U. W. Paetzold, G. Hernández-Sosa, R. Kling, U. Lemmer, *Nat. Commun.* **2024**, *15*, 3372.
[14] J. Heo, I. Jung, H. Park, J. H. Han, H. Kim, H. Park, J.-S. Park, H. Jeon, K.-T. Lee, H. W. Baac, H. J. Park, *Adv. Opt. Mater.* **2021**, *10*, 2101696.
[15] S. Bae, S. Bae, Y. W. Noh, Y. W. Noh, D.-S. Park, D.-S. Park, M. H. Song, M. H. Song, S.-W. Choi, S.-W. Choi, *Nano Energy* **2021**, *93*, 106801.
[16] H. Eggers, S. Gharibzadeh, S. Koch, F. Schackmar, D. Ritzer, T. Abzieher, B. S. Richards, C. Erban, U. W. Paetzold, *Sol. RRL* **2022**, *6*.
[17] G. Y. Yoo, R. Azmi, C. Kim, W. Kim, B. K. Min, S.-Y. Jang, Y. Rag, *ACS Nano* **2019**, *13*, 10129.
[18] A. Magomedov, A. Al-Ashouri, E. Kasparavičius, S. Strazdaite, G. Niaura, M. Jošt, T. Malinauskas, S. Albrecht, V. Getautis, *Adv. Energy Mater.* **2018**, *8*, 1801892.
[19] A. Al-Ashouri, A. Magomedov, M. Ros, M. Jošt, M. Talaikis, G. Chistiakova, T. Bertram, J. A. Márquez, E. Köhnen, E. Kasparavičius, S. Levcenco, L. Gil-Escrig, C. J. Hages, R. Schlatmann, B. Rech, T. Malinauskas, T. Unold, C. A. Kaufmann, L. Korte, G. Niaura, V. Getautis, S. Albrecht, *Energy Environ. Sci.* **2019**, *12*, 3356.
[20] A. Al-Ashouri, E. Köhnen, B. Li, A. Magomedov, H. Hempel, P. Caprioglio, J. A. Márquez, A. B. M. Vilches, E. Kasparavicius, J. A. Smith, N. Phung, D. Menzel, M. Grischek, L. Kegelmann, D. Skroblin, C. Gollwitzer, T. Malinauskas, M. Jošt, G. Matič, B. Rech, R. Schlatmann, M. Topič, L. Korte, A. Abate, B. Stannowski, D. Neher, M. Stolterfoht, T. Unold, V. Getautis, S. Albrecht, *Science* **2020**, *370*, 1300.
[21] R. Santbergen, T. Meguro, T. Suezaki, G. Koizumi, K. Yamamoto, M. Zeman, *IEEE J. Photovoltaics* **2017**, *7*, 919.
[22] D. Yoo, P. Tillmann, T. Kraus, J. Sutter, A. Harter, S. Trofimov, B. Naydenov, K. Jäger, H. Hauser, C. Becker, *Sol. RRL* **2023**, *7*, 2300071.
[23] E. I. Stearns, *Color Res. Appl.* **1988**, *13*, 64.
[24] G. Sharma, W. Wu, E. N. Dalal, *Color Res. Appl.* **2005**, *30*, 21.

[25] T. Mansencal, M. Mauderer, M. Parsons, N. Shaw, K. Wheatley, S. Cooper, J. D. , L. Canavan, K. Crowson, O. Lev, K. Leinweber, S. Sharma, T. J. Sobotka, D. Moritz, M. Pppp, C. Rane, P. Eswaramoorthy, J. Mertic, B. Pearlstine, M. Leonhardt, O. Niemitalo, M. Szymanski, M. Schambach, S. Huang, M. Wei, N. Joywardhan, O. Wagih, P. Redman, J. Goldstone, S. Hill, et al., Colour 0.4.4. Version 0.4.4 **2023**.
[26] P.-I. Schneider, X. G. Santiago, V. Soltwisch, M. Hammerschmidt, S. Burger, C. Rockstuhl, *ACS Photonics* **2019**, *6*, 2726.
[27] P.-I. Schneider, In Preparation **2024**.